IJMMM International Journal of Minerals, Metallurgy and Materials 矿物冶金与材料学报（英文版）

Microstructure and mechanical properties of high-strength low alloy steel by wire and arc additive manufacturing

Yi-li Dai, Sheng-fu Yu, An-guo Huang, and Yu-sheng Shi

Cite this article as:
Yi-li Dai, Sheng-fu Yu, An-guo Huang, and Yu-sheng Shi, Microstructure and mechanical properties of high-strength low alloy steel by wire and arc additive manufacturing, *Int. J. Miner. Metall. Mater.*, 27(2020), No. 7, pp. 933-942. https://doi.org/10.1007/s12613-019-1919-1

International Journal of Minerals, Metallurgy and Materials
Volume 27, Number 7, July 2020, Page 933
https://doi.org/10.1007/s12613-019-1919-1

Microstructure and mechanical properties of high-strength low alloy steel by wire and arc additive manufacturing

Yi-li Dai, Sheng-fu Yu, An-guo Huang, and Yu-sheng Shi

State Key Laboratory of Material Processing and Die & Mould Technology, Huazhong University of Science and Technology, Wuhan 430074, China
(Received: 22 July 2019; revised: 26 September 2019; accepted: 27 September 2019)

Abstract: A high-building multi-directional pipe joint (HBMDPJ) was fabricated by wire and arc additive manufacturing using high-strength low-alloy (HSLA) steel. The microstructure characteristics and transformation were observed and analyzed. The results show that the forming part includes four regions. The solidification zone solidifies as typical columnar crystals from a molten pool. The complete austenitizing zone forms from the solidification zone heated to a temperature greater than 1100°C, and the typical columnar crystals in this zone are difficult to observe. The partial austenitizing zone forms from the completely austenite zone heated between Ac1 (austenite transition temperature) and 1100°C, which is mainly equiaxed grains. After several thermal cycles, the partial austenitizing zone transforms to the tempering zone, which consistes of fully equiaxed grains. From the solidification zone to the tempering zone, the average grain size decreases from 75 to 20 μm. The mechanical properties of HBMDPJ satisfies the requirement for the intended application.

Keywords: wire and arc additive manufacturing; high strength low alloy steel; microstructure; inclusions; fine grain ferrite; mechanical properties

1. Introduction

High-building multidirectional pipe joints (HBMDPJs) are a critical part in high building structures, and the mechanical properties of HBMDPJs directly influence the safety of high buildings [1]. A HBMDPJ is usually composed of several pipes from different directions and bear different loads from different directions [2]. At least six intersecting pipes are required to form a HBMDPJ, and the intersecting surfaces are complex spatial surfaces that are difficult to fabricate. Currently, the main method used to form HBMDPJs is casting [3–4]. However, casting defects, such as shrinkage and pores, are easily introduced, and it`s difficult to ensure the high performance of the casting part. At the same time, a HBMDPJ is single product [5] whose structure varies at different positions in one high building; in such cases, the casting flow is long and the production cost is very high.

Wire and arc additive manufacturing (WAAM) is a novel forming method which selects arc as a heat source to melt metal wire and deposits metal layer by layer to fabricate a metal structure [6]. WAAM enables the fabrication of complex structures by transforming a three-dimensional structure into a two-dimensional layer structure. It has the advantages of a high forming efficiency, high material utilization, and the ability to form arbitrarily complex space surface structures [7–9]. Therefore, WAAM is an effective method to fabricate HBMDPJs.

The HBMDPJ is designed to withstand various static and dynamic loads that require high stability with good strength and toughness. The mechanical properties of a forming part are directly influenced by its microstructure. In order to fabricate pipe joints with excellent mechanical properties, the microstructure and phase transformation of the material should be controlled. Compared with traditional manufacturing methods, WAAM is a reciprocating heating process in which the formed part undergoes several thermal cycles, resulting in a special microstructure. Fachinotti *et al*. [10] established finite-element modeling to analyze heat transformation in shape-metal deposition. During the deposition process, the forming part is subjected repeatedly to high heating and cooling rates, which results in unique morphologies and microstructures. Ge *et al*. [11] studied the effect of thermal history on the microstructure and mechanical properties of 2Cr13 steel prepared by WAAM. They found that the cooling rate first decreases quickly and then remains stable in layers 15 to 25 during deposition and that the amount of

Corresponding author: Sheng-fu Yu E-mail: yushengfu@hust.edu.cn

martensite increases gradually from layer 5 to 15. Asala *et al.* [12] analyzed the microstructure development of 718Plus during WAAM in detail. They found that the peak temperature of thermal cycling varies by position. Other regions under the top layer experience heat treatment from the post-deposition layer, which causes some of the eutectic particles to dissolve into the γ-matrix and influence the mechanical properties of the resultant steel. Chen *et al.* [13] investigated the microstructure and mechanical properties of austenite stainless steel 316L fabricated by WAAM. They found that, with increasing number of layers, the peak temperature decreases from the γ-phase zone temperature to 600°C. Under different peak temperatures, the δ phase gradually dissolves into the γ phase and σ phase and the microstructure changes from a reticular morphology to a fine vermicular morphology. The microhardness of the forming part increases from top to bottom. Wang *et al.* [14] researched the effect of location on the microstructure and mechanical properties of Inconel 625 prepared by WAAM. They demonstrated that the previous layer undergoes several different thermal cycles, which influences the segregation behavior of Nb and Mo. The contents of Nb and Mo directly affect the Laves-phase content, which causes the microhardness and tensile strength to vary at different positions.

Numerous researchers have investigated the microstructure and mechanical properties of stainless steel, ATI 718, and Inconel 625 fabricated by WAAM. However, few researchers have studied the microstructure and mechanical properties of high-strength low alloy (HSLA) steel structural parts fabricated by WAAM. Rodrigues *et al.* [15] studied the effect of thermal cycling on the microstructure and mechanical properties of HSLA steel, investigating the influence of heat input on the grain size of the forming part. However, the transformation mechanism and characteristics of the HSLA steel's microstructure were not investigated.

Therefore, in the present paper, we measured the temperature field and thermal cycle during WAAM, analyzed the characteristics and transformation of the microstructure, and tested the mechanical properties of the formed part. The experimental results provide basic data for fabricating high performance, complex HSLA structures such as HBMDPJs.

2. Experimental

HSLA wire was used to fabricate a HBMDPJ by WAAM, and the diameter of the wire was 1.2 mm; the chemical composition of the deposited part is shown in Table 1. The equipment for WAAM was a KUKA KR30-3HA robot and a Fronius CMT (cold metal transfer) arc welding power source. The process was conducted under an arc current of 130–140 A, arc voltage range of 18–20 V, and torch travel speed of 7–8 mm/s. The shielding gas was CO_2, and the flow rate was 15–20 L/min. During deposition, the inner and outer contours of pipes were formed first and then the center portion was filled by equal-thickness offsetting. The offsetting distance was approximately 4–5 mm. A K-type (nickel chromium–nickel silicon) thermocouple was welded onto the top layer of the deposited metal, and the thermal cycle curves were gathered.

Table 1. Chemical composition of depositing part wt%

C	Mn	Si	Cr	Ni	Mo	Zr	S	P	Fe
0.08	1.40	0.78	0.30	0.70	0.50	0.009	0.001	0.001	Bal.

To analyze the distribution of temperature of the forming part during deposition clearly, we simulated the temperature field using the software ABAQUS. The heating source is described using the double-ellipsoidal model [16] (Fig. 1), and the heat input rate density pre-unit volume is calculated by Eqs. (1)–(2).

$$q_f(x,y,z) = \frac{6\sqrt{3}f_f Q}{a_f b_h c_h \pi\sqrt{\pi}} e^{\left(-\frac{3x^2}{a_f^2}-\frac{3y^2}{b_h^2}-\frac{3z^2}{c_h^2}\right)}, \quad x \geqslant 0 \tag{1}$$

$$q_r(x,y,z) = \frac{6\sqrt{3}f_r Q}{a_r b_h c_h \pi\sqrt{\pi}} e^{\left(-\frac{3x^2}{a_r^2}-\frac{3y^2}{b_h^2}-\frac{3z^2}{c_h^2}\right)}, \quad x < 0 \tag{2}$$

where q_f and q_r are the heat flux density of the front and the rear; Q is the total heat input; f_f and f_r are the portion of heat distributed in the front and rear semi-ellipsoid, where $f_f + f_r = 2$; a_f (or a_r), b_h, and c_h are the semi-axes of the front (or rear) semi-ellipsoid.

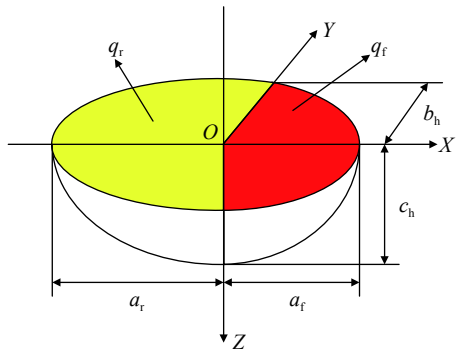

Fig. 1. Schematic diagram of double ellipsoid model. *X* is the direction of the arc movement, *Y* is the radial direction of the pipe, *Z* is the vertical direction, and *O* is origin.

During the deposition, the size of forming part is much larger than that of the arc. Heat exchange occurs through two main mechanisms: heat convection and heat radiation [17].

The corresponding thermal boundary conditions are:

$$\lambda\frac{\partial T}{\partial \boldsymbol{n}} = h(T - T_0) \tag{3}$$

$$\lambda\frac{\partial T}{\partial \boldsymbol{n}} = \varepsilon\sigma\left(T^4 - T_0^4\right) \tag{4}$$

where $\boldsymbol{n}$ is the boundary normal vector, λ is the thermal conductivity of the material ($W\cdot m^{-1}\cdot K^{-1}$), h is the heat transfer coefficient ($W\cdot m^{-2}\cdot K^{-1}$), T and T_0 are temperature of the forming part and the surrounding environment (K), respectively, ε is the surface emissivity of forming part, and σ is the Stefan–Boltzmann constant (5.67×10^{-8} $W\cdot m\cdot K^{-4}$). The other thermophysical parameters were calculated using the JMatPro software. To verify the results of the simulation, a thermal infrared (IR) camera was used to capture the real-time temperature of the forming part during deposition. The temperature range was set to 200–2000°C, and the frame rate was 15 Hz.

Metallographic specimens were cut from the depositing part using an electric discharge wire, followed by standard mechanical polishing and etching with nitric acid alcohol solution (4 mL HNO_3 and 96 mL C_2H_6O). The microstructure was observed by optical microscopy (OM) and scanning electron microscopy (SEM). A Tecnai G2 F30 field-emission transmission electron microscope was used to observe and analyze the microstructure and metallographic structure.

To observe the austenitization process *in situ*, high-temperature laser scanning confocal microcopy (HTLSCM) was conducted. The disc samples with 7 mm in diameter and 3 mm in thickness were cut from the depositing metal. Two samples were heated at a rate of 16.7°C·s^{-1} to 1350°C and maintained for 5 s. The corroded samples, which is etched with nitric acid alcohol solution (4 mL HNO_3 and 96 mL C_2H_6O), and the uncorroded samples were used to observe the transformation and grain growth of austenite, respectively.

The specimens for mechanical tests were removed from the deposited part, and the direction was horizontal (arc gun movement direction) and vertical (perpendicular to the direction of arc gun movement). The equipment included an AG-IC 100 kN tensile testing machine and a ZBC3302-A Charpy impact machine, and the tensile and impact testing standards were ASTM E8M and ASTM E32, respectively. After mechanical testing, the fracture morphologies of the specimens were observed by SEM.

3. Results and discussion

3.1. Temperature field and thermal cycle

3.1.1. Temperature field

Fig. 2(a) shows the actual temperature distribution of the forming part during the deposition measured by the IR camera, and Fig. 2(b) shows the simulation results by software. According to the isotherms and temperature values of corresponding positions in these two figures, the temperature profile obtained by thermal simulation is consistent with the actual temperature distribution during the deposition. Therefore, the numerical simulation results could be used to analyze the temperature distribution during the deposition.

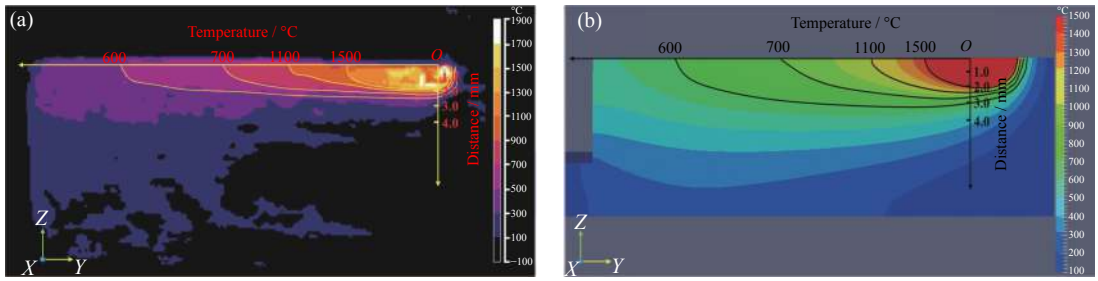

Fig. 2. ***In situ*** **temperature field by measurement and simulation, corresponding to the lateral direction: (a) measurement result by infrared thermography; (b) simulation result.**

As shown in Fig. 2, during deposition, the maximum depth of the molten pool (>1500°C) is 2.0 mm, where liquid metal solidifies and crystallizes to form a solidified structure in what is known as the solidification zone. The other region below the molten pool is the heat-affected zone (HAZ), where the temperature is greater than Ac1(austenite transition temperature). The depth range of the HAZ ranges from 2.0 to 3.5 mm, as shown in Fig. 2(b). According to iron and carbon phase diagram, the microstructure of HSLA steel undergoes different transformations at different temperatures. Therefore, the HAZ can be divided into three regions.

As shown in Fig. 2, the temperature ranges from 1100 to 1500°C in the depth range from 2.0 to 2.5 mm. The microstructure of this zone is formed form the solidification zone. The HTLSCM was used to simulate the thermal cycle to observe the microstructure transformation during the heating, and the results is shown in Figs. 3(e)–3(i). As shown in Figs. 3(f) and 3(g), when the temperature reaches 1050°C, the proportion of austenite is just 90%; only when the temperature reaches 1100°C, the proportion of austenite is greater than 98%. It's can be seen that only when the temperature is higher than 1100°C, the microstructure will transform to austen-

ite completely. Therefore, this region is called the complete austenitizing zone.

The temperature ranges from Ac1 to 1100°C in the depth range from 2.5 to 3.5 mm. In this region, the solidification undergoes two thermal cycles; however, the temperature of second heating is insufficient to promote complete austenitization, and the proportion of austenite is only ~50% (Fig. 3(h)). This region is called the partial austenitizing zone.

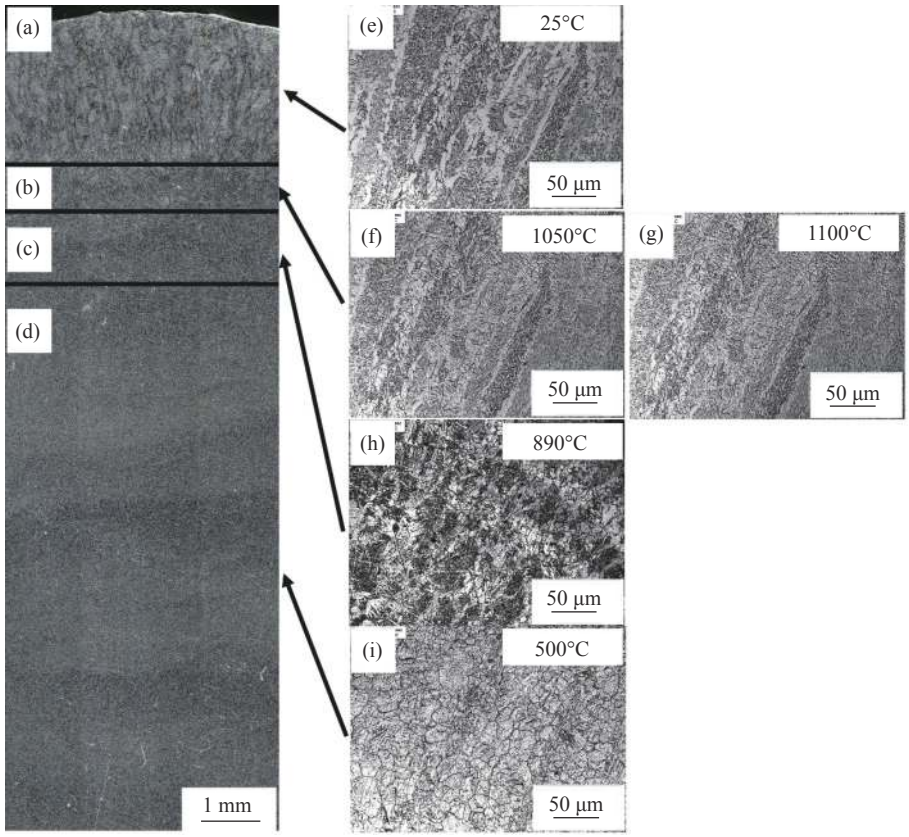

Fig. 3. (a–d) The microstructure distribution of the forming part and (e–i) the microstructure transformation of the solidification zone after the different number of thermal cycles observed by HTLSCM : (e) before thermal cycle, corresponding to the (a); (f, g) after one thermal cycle, corresponding to the (b); (h) after two cycles, corresponding to the (c); (i) after three cycles, corresponding to the (d).

At depths below 3.5 mm, the temperature is less than Ac1. In this region, the solidification undergoes three thermal cycles but the phase transformation does not occur and the microstructure is characterized by equiaxed crystals (Fig. 3(i)). This region is called the tempering zone.

Therefore, the HSLA structure formed by WAAM could be divided into four regions (Fig. 3): the solidification zone, complete austenitizing zone, partial austenitizing zone, and the tempering zone (Figs. 3(a)–3(d)). The microstructure and crystal structure in each region exhibit distinctly different characteristics.

3.1.2. Thermal cycles

Fig. 4(a) shows a schematic of the thermal cycles, and point A is the measurement point. Fig. 4(b) is the thermal cycle curves of point A after deposition of five layers. After the base layer is deposited, point A is formed via liquid-metal solidification in the solidification zone. During deposition of subsequent layers, point A experiences thermal cycles with distinct peak temperatures. When the first layer is deposited, the peak temperature of point A is 1250°C, which is between 1100 and 1500°C. The solidification zone undergoes complete austenitization, and point A transfers from the solidification zone to the complete austenitizing zone. During deposition of the second layer, the peak temperature is 890°C, which is between Ac1 and 1100°C. The microstructure shows incomplete austenitization [18], and only pearlite (P) transforms to austenite. Point A transfers from the complete austenitizing zone to the partial austenitizing zone. During deposition of the third and subsequent layers, the peak temperature is less than 650°C, which is less than Ac1. The subsequent deposition is equivalent to a tempering heat treatment, and the microstructure becomes homogenized. Point A transfers from the partial austenitizing zone to the tempering zone. In conclusion, point A experiences continuous solidification, complete austenitizing, partial austenitizing, and finally becomes a tempering zone, as shown in Fig. 4(a).

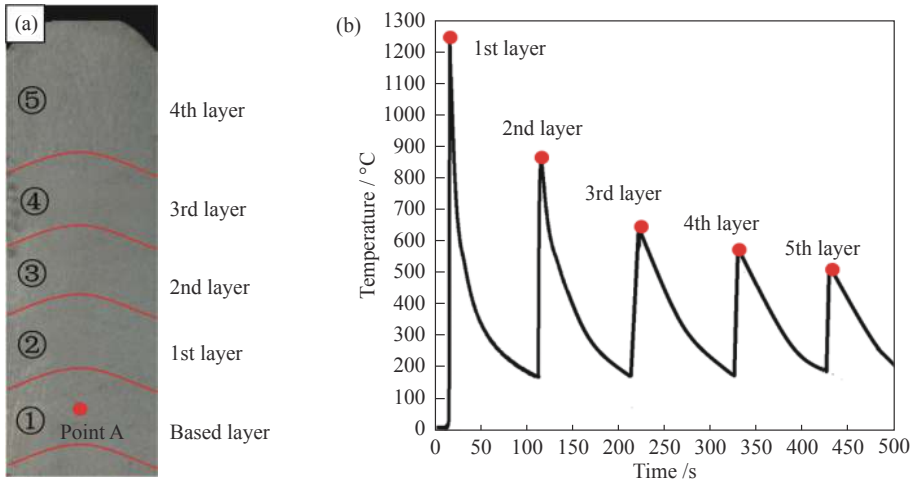

In the beginning, ① is based layer, which is the solidification zone;
When depositing lst layer, ① is complete austenitizing zone;
When depositing 2nd layer, ① is partial austenitizing zome and ② is complete austenitizing zone;
When depositing 3rd layer, ① is tempering zone, ② is partial austenitizing zone, and ③ is complete austenitizing zone;
When depositing 4th layer, ① and ② are tempering zone, ③ is partial austenitizing zone, and ④ is complete austenitizing zone.

Fig. 4. (a) Schematic of thermal cycles and (b) thermal cycle curve of point A in (a).

Furthermore, these four regions exist simultaneously in the sublayers under the depositing layer, where they experience different thermal cycles, resulting in distinct microstructure characteristics and phase transformations. These differences in microstructure and phase transformation will strongly affect the mechanical properties of the forming part fabricated by WAAM.

3.2. Microstructure of depositing part

3.2.1. Solidification zone

Micrographs of the microstructure in the solidification zone are shown in Fig. 5. The crystals forming the solidification zone are columnar crystals with a certain orientation. The average width of the columnar crystals is approximately 75 μm. The molten pool of WAAM is very small (Fig. 2(b)), and the cooling speed is extremely high. According to the thermal cycle in Fig. 4, during deposition of the first layer, the cooling rate reaches 120–150°C/s. A large number of grains nucleate and rapidly grow, and the columnar crystals generate preferentially along the direction of highest cooling rate in the solidification zone.

The microstructure of the solidification zone is composed of pro-eutectoid ferrite (PF), ferrite side plate (FSP), and acicular ferrite (AF), as shown in Fig. 5(a). The PF locates at the boundary of austenite, and the FSP forms vertical to the grain boundary. Much AF is present in the microstructure of the forming part, as shown in Fig. 5(b). AF is an ideal microstructure for improving the toughness of HSLA steel. In the solidification zone, the presence of numerous AF grains would improve its strength and toughness, thereby ensuring good mechanical properties of the solidification zone.

Fig. 6 shows the SEM and TEM micrographs of inclusions in the solidification zone. As evident in Fig. 6(a), the AF forms on the surface of inclusions, which are composed of elements Zr, Al, Mn, Si, S, and O, indicating that the main components of the compounds were $ZrO_2 \cdot Al_2O_3 \cdot MnO \cdot SiO_2 \cdot MnS$, as shown in Fig. 6(b). The core of the inclusions is composed of ZrO_2, and the other oxides precipitated on the surface. Pu *et al*. [19] and Guo *et al*. [20] have reported similar results. This precipitation behavior is attributed to the

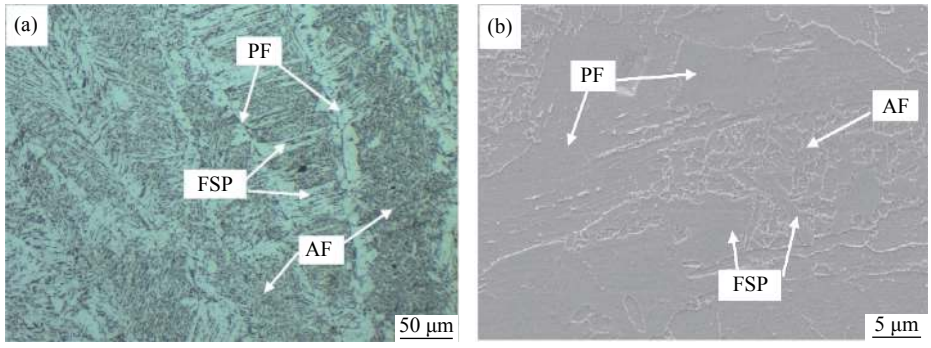

Fig. 5. Micrograph of solidification zone: (a) OM image; (b) SEM image.

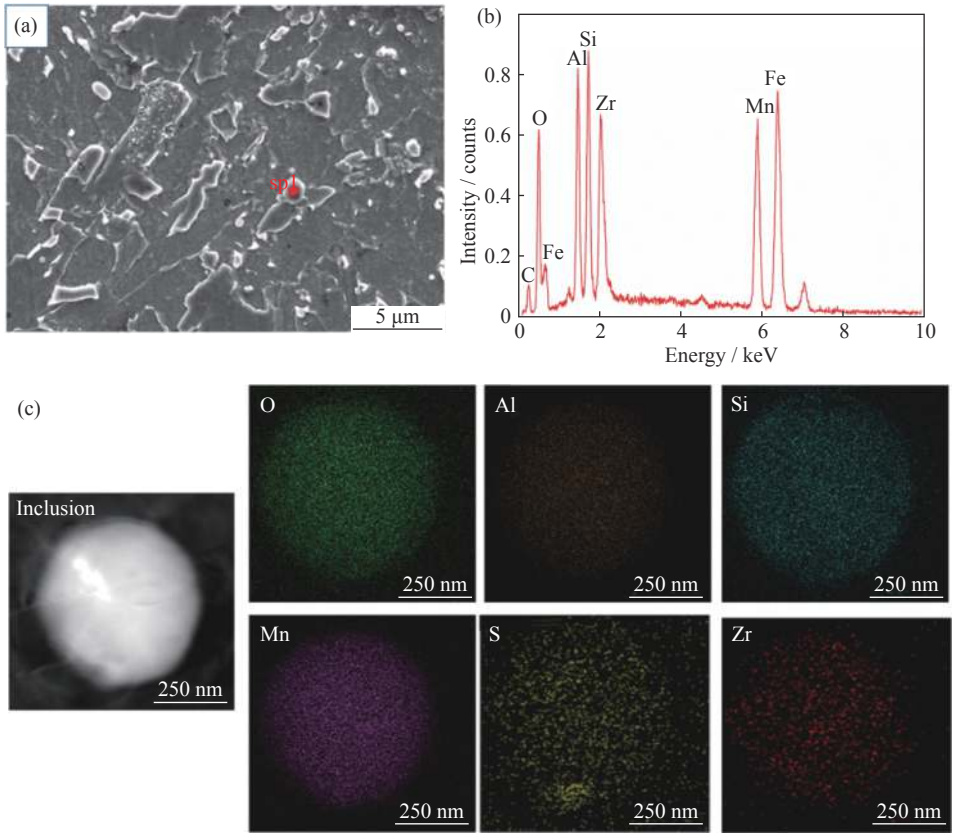

Fig. 6. SEM and TEM micrographs of inclusions in the solidification zone: (a) SEM image; (b) EDS spectrum of point sp1 in (a); (c) TEM–EDS mapping images.

forming part being alloyed by Zr, which is a strong deoxidizing element and first reacts with oxygen to form ZrO_2 during cooling. The ZrO_2 particles provide nucleation cores for other oxides. The composite inclusions $ZrO_2{\cdot}Al_2O_3{\cdot}MnO{\cdot}SiO_2{\cdot}MnS$ in the solidification zone promote the nucleation of AF, as shown in Fig. 7. Therefore, the microstructure of the solidification zone contains PF, FSP, and a large amount of AF.

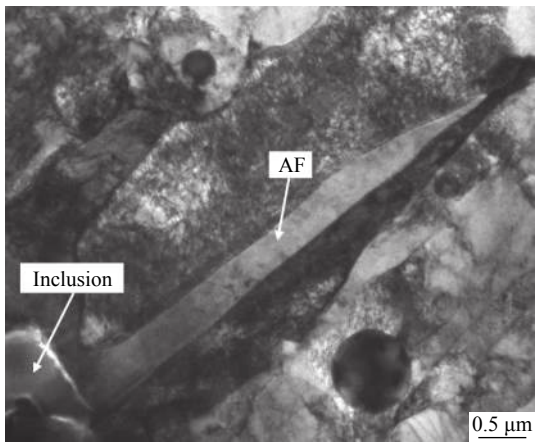

Fig. 7. TEM micrograph of inclusion-induced AF in solidification zone.

3.2.2. Complete austenitizing zone

Micrographs of the microstructure in the complete austenitizing zone are shown in Fig. 8. These images show that the columnar crystals become unclear and that some equiaxed grains appear in the complete austenitizing zone. The average grain size is approximately 70 μm, which is smaller than the grain size in the solidification zone. During the first thermal cycle, the solidification zone changes to the complete austenitizing zone and the microstructure would be complete austenitization.

Fig. 9 shows *in situ* observations of the growth of austenite grains during heating from 1100 to 1250°C. Compared with the grains in zone 1 and zone 2 in Fig. 9, when the temperature increased from 1100 to 1250°C, no distinct coarsening of prior austenite grains was observed because large numbers of inclusions locate in the austenite grain boundaries and the pinning effect of composite inclusions hinders the growth of austenite grains, as shown in Fig. 10.

The microstructure of the complete austenitizing zone includes PF, FSP, AF, and a small amount of fine grain ferrite (FGF), as shown in Fig. 8. Compared with the solidification zone, the PF and FSP contents decrease, whereas the proportion of AF increases. Because of the refinement of prior austenite grains, the growth of PF and FSP is limited; they cannot fully grow and transform into small-sized ferrite.

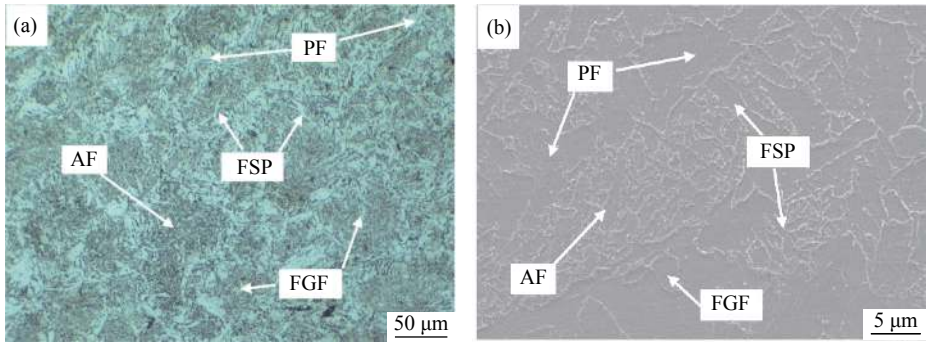

Fig. 8. Micrographs of the microstructure in the complete austenitizing zone: (a) OM image; (b) SEM image.

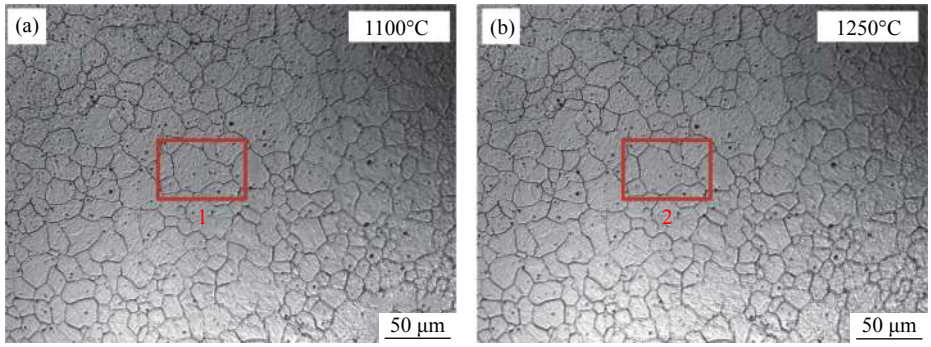

Fig. 9. *In situ* observation photo of austenite grains by HTLSCM: (a) 1100°C; (b) 1250°C.

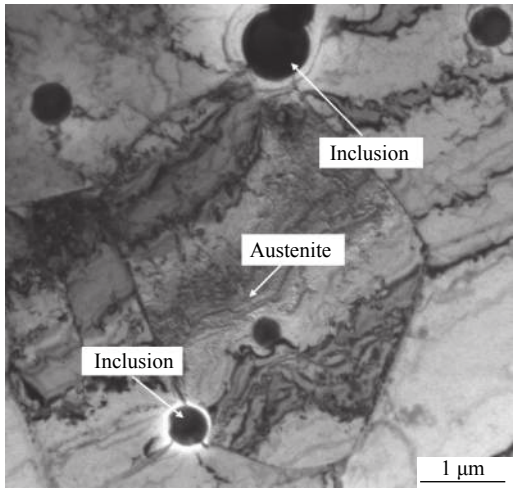

Fig. 10. TEM micrograph of composite inclusions at the boundary in the complete austenitizing zone.

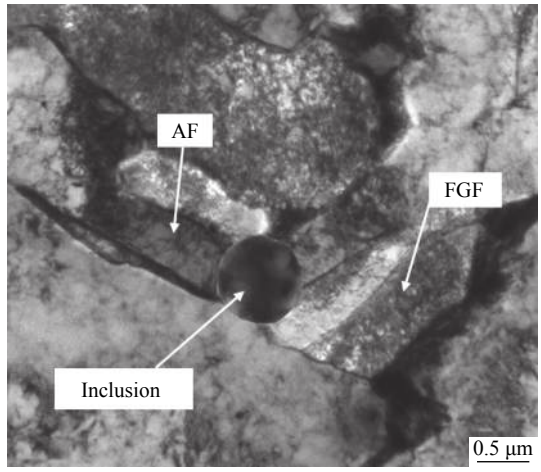

Fig. 11. TEM micrograph of AF in the complete austenitizing zone.

In addition, during the first thermal cycle, the existing composite inclusions form inside austenite again and induce intragranular AF nucleation. The content of intragranular AF increases. The increasing of AF causes the interlocking phenomenon, which limits the growth of some AF and makes the AF gradually transforms into FGF, as shown in Fig. 11. At the same time, when the temperature decreases to 500°C, the FGF forms in the austenite grains [21]. Therefore, the proportion of AF and FGF in the complete austenitizing zone increases.

3.2.3. Partial austenitizing zone

Fig. 12 shows micrographs of the microstructure in the partial austenitizing zone. The columnar crystals have disappeared, and equiaxed grains are mainly present. The average size is approximately 40 μm. Compared with the complete austenitizing zone, the partial austenitizing zone contains less PF, FSP, and AF but more FGF.

In the partial austenitizing zone, the composite inclusions composed of $ZrO_2 \cdot Al_2O_3 \cdot MnO \cdot SiO_2 \cdot MnS$ still limit the growth of austenite grains and induce the nucleation of AF. Therefore, the PF and FSP contents decrease compared with

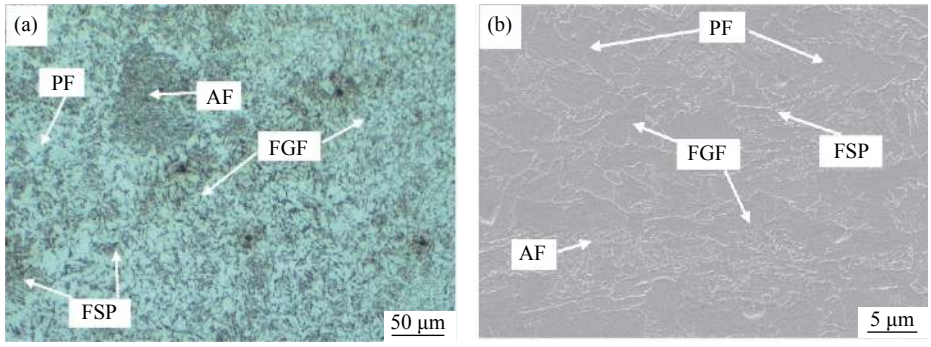

Fig. 12. Micrographs of the microstructure in the partial austenitizing zone: (a) OM image; (b) SEM image.

those in the complete austenitizing zone, whereas a large amount of AF forms in the prior austenite grains. These large amounts of intragranular AF restrict each other, and cannot grow up sufficiently. These intragranular AF will transform to FGF, and the content of FGF will increase. The content of FGF increases and one austenite grain transforms into several intragranular ferrite grains, which results in refinement of the grain size. At the same time, the microstructure gradually transforms from columnar crystals into equiaxed grains, as shown in Fig. 13.

3.2.4. Tempering zone

Fig. 14 shows micrographs of the microstructure in the tempering area. The structure is composed of fine equiaxed grains with an average size of approximately 20 μm. The microstructure is composed of FGF and a small amount of P, and the P forms on the grain boundary of the FGF, as shown

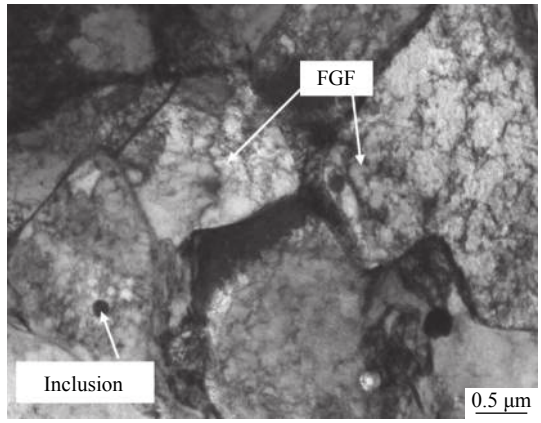

Fig. 13. TEM microstructure of FGF in the partial austenitizing zone.

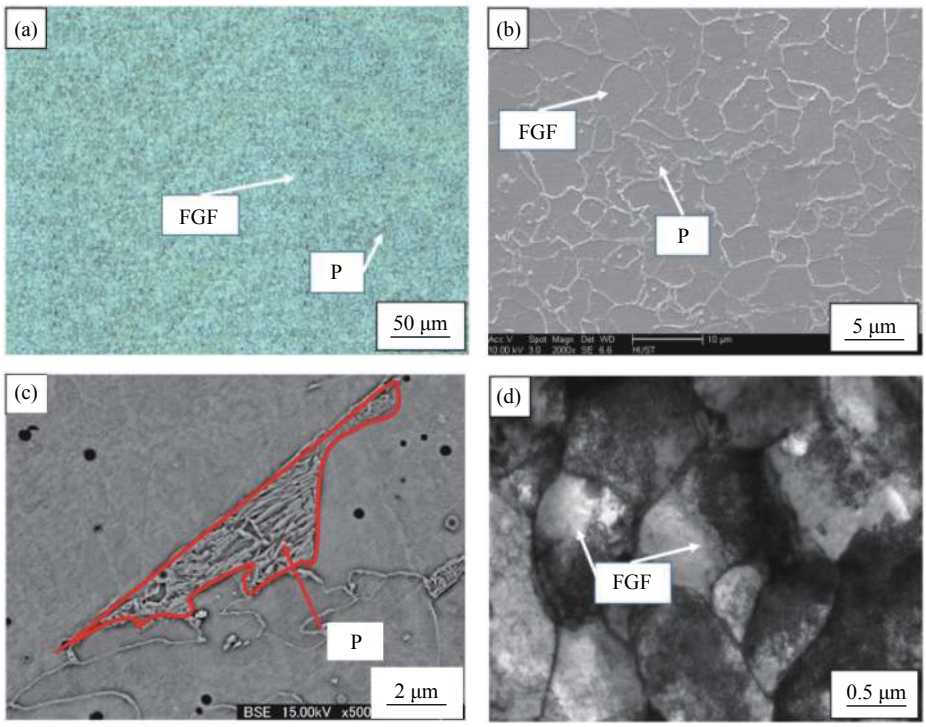

Fig. 14. Micrographs of the microstructure in the tempering zone: (a) OM image; (b) SEM image; (c) SEM image of P; (d) TEM image of FGF.

in Fig. 14(c). Compared with the size of the equiaxed grains and the average grain size in the partial austenitizing zone, those in the tempering zone are smaller.

WAAM is characterized by rapid heating and cooling. During the rapid heating process, ferrite transforms into austenite, although some un-austenitized ferrite nuclei remain in the austenite grains. When the temperature falls below 500°C [21], the ferrite nuclei promote the nucleation and growth of FGF in prior austenite grains. The presence of numerous nuclei promotes FGF formation, and the grain size is refined.

Furthermore, after the deposition of the third and subsequent layers, some supercooled austenite still remains in the tempering zone because of the rapid cooling. At the same time, the heat accumulation of WAAM maintains the temperature between 250 and 550°C for an extended period, as shown in Fig. 14(b). When the temperature remains at 350–550°C for an extended period, the supercooled austenite decomposes into P and ferrite [22]. Therefore, some P forms in the tempering zone.

3.3. Mechanical properties

The mechanical properties of the forming part were tested and found to be comparable to those of the casting part. The results are listed in Table 2. According to the measurement results, the mechanical properties of depositing part are not worse than those of the casting part with the same chemical composition.

Table 2. Mechanical properties of the forming part in different directions and casting part

Sample	Direction	Tensile strength, R_m / MPa	Yield strength, R_p / MPa	Elongation, δ / %	Impact toughness, A_k / J (at 20°C)
Casting	Average	≥500	≥300	≥22	≥60
Depositing	Horizontal	580	420	27.5	112
	Vertical	548	414	25.5	104
	Average	564	417	26.5	108

The strength of HSLA steel depends on the average grain size of the forming part [23]. After subsequent thermal cycles, the average size of the grains was refined. The average size of the tempering zone was less than 20 μm, and the mechanical properties of the forming part were excellent.

Fig. 15 shows high-magnification images of a tensile and an impact toughness fractures of the forming part. The tensile and impact toughness fracture surfaces both consist of numerous small dimples, which indicates that the fracture type is ductile fracture. The impact toughness and tensile values of HBMDPJs fabricated by WAAM are good.

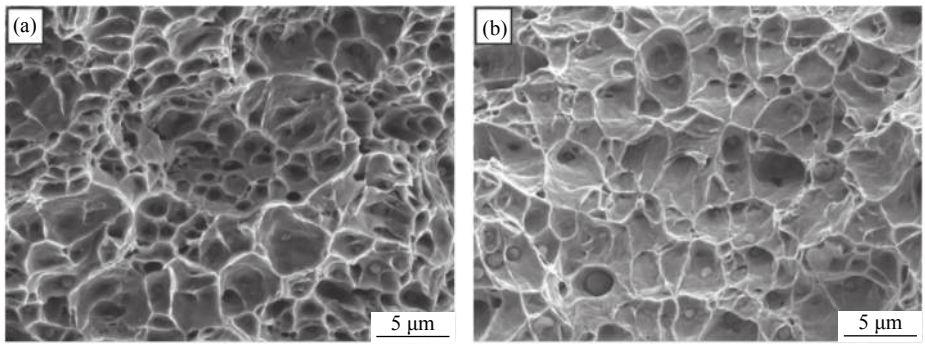

Fig. 15. Fracture photos of the forming part: (a) tensile fracture; (b) impact toughness fracture.

4. Conclusions

In this study, a HBMDPJ was successfully fabricated by WAAM. The characteristics of different parts were observed, and the phase transformation was analyzed. At the same time, the mechanical properties were tested. The following conclusions were drawn.

(1) HBMDPJs can be fabricated by WAAM, and the forming part includes four regions: a solidification zone, complete austenitizing zone, partial austenitizing zone, and a tempering zone.

(2) Under several thermal cycles, each position of the part formed by WAAM transitions from the solidification zone, to the complete austenitizing zone, partial austenitizing zone, and finally the tempering zone. The crystals transform from typical columnar crystals in the solidification zone to fine equiaxed grains in the tempering zone.

(3) The $ZrO_2{\cdot}Al_2O_3{\cdot}MnO{\cdot}SiO_2{\cdot}MnS$ in the HBMDPJ plays a critical role in the transformation of its microstructure. The inclusions not only obstruct the growth of austenite but also induce the nucleation of AF to refine the grain size and promote the transformation of PF, FSP, and AF to FGF.

(4) The microstructure of the HBMDPJ consists of FGF and P, and the average grain size is less than 20 μm. The

tensile strength is 564 MPa, the yield strength is 417MPa, the elongation is 26.5%, and the impact toughness is 108 J at 20°C. The mechanical properties of the formed part are excellent.

Acknowledgements

This work was financially supported by the National Key R&D Program of China (No. 2017YFB1103200) and the Independent Innovation Research Fund Project of Huazhong University of Science and Technology (No. 2018KFYXMPT002).

References

[1] S. Herion, J.C. de Oliveira, J.A. Packer, C. Christopoulos, and M.G. Gray, Castings in tubular structures—The state of the art, *Proc. Inst. Civ. Eng. Struct. Build.*, 163(2010), No. 6, p. 403.

[2] J. Xia and H. Jin, Analysis of residual stresses and variation mechanism in dissimilar girth welded joints between tubular structures and steel castings, *Int. J. Press. Vessels Pip.*, 165(2018), p. 104.

[3] J.P. Liu and J. Wei, Study on casting process of cast steel joints for buildings, *Hot Working Technol.*, 44(2015), No. 5, p. 13.

[4] J.C. de Oliveira, J.A. Packer, and C. Christopoulos, Cast steel connectors for circular hollow section braces under inelastic cyclic loading, *J. Struct. Eng.*, 134(2008), No. 3, p. 374.

[5] L.X. Lu, Discussion on application of cast-steel node in lager-span pipe truss architecture steel structure, *Steel Constr.*, 18(2003), No. 5, p. 28.

[6] D.H. Ding, Z.X. Pan, D. Cuiuri, and H.J. Li, Wire-feed additive manufacturing of metal components: Technologies, developments and future interests, *Int. J. Adv. Manuf. Technol.*, 81(2015), No. 1-4, p. 465.

[7] J.S. Panchagnula and S. Simhambhatla, Manufacture of complex thin-walled metallic objects using weld-deposition based additive manufacturing, *Rob. Cimput. Integr. Manuf.*, 49(2018), p. 194.

[8] Y.Y. Lei, J. Xiong, and R. Li, Effect of inter layer idle time on thermal behavior for multi-layer single-pass thin-walled parts in GMAW-based additive manufacturing, *Int. J. Adv. Manuf. Technol.*, 96(2018), No. 1-4, p. 1355.

[9] P. Kazanas, P. Deherkar, P. Almeida, H. Lockett, and S. Williams, Fabrication of geometrical features using wire and arc additive manufacture, *J. Eng. Manuf.*, 226(2012), No. 6, p. 1042.

[10] V.D. Fachinotti, A. Cardona, B. Baufeld, and O.V. der Biest, Finite-element modelling of heat transfer in shaped metal deposition and experimental validation, *Acta. Mater.*, 60(2012), No. 19, p. 6621.

[11] J.G. Ge, J. Lin, Y.P. Lei, and H. G. Fu, Location-related thermal history, microstructure, and mechanical properties of arc additively manufactured 2Cr13 steel using cold metal transfer welding, *Mater. Sci. Eng. A*, 715(2018), p. 144.

[12] G. Asala, A.K. Khan, J. Andersson, and O.A. Ojo, Microstructural analyses of ATI 718Plus produced by wire-arc additive manufacturing process, *Metall. Mater. Trans. A*, 48(2017), No. 9, p. 4211.

[13] X.H. Chen, J. Li, X. Cheng, B. He, H.M. Wang, and Z. Huang, Microstructure and mechanical properties of the austenitic stainless steel 316L fabricated by gas metal arc additive manufacturing, *Mater. Sci. Eng. A*, 703(2017), p. 567.

[14] J.F. Wang, Q.J. Sun, H. Wang, J.P. Liu, and J.C. Feng, Effect of location on microstructure and mechanical properties of additive layer manufactured Inconel 625 using gas tungsten arc welding, *Mater. Sci. Eng. A*, 676(2016), p. 395.

[15] T.A. Rodrigues, V. Duarte, J.A. Avila, T.G. Santos, R.M. Miranda, and J.P. Oliveira, Wire and arc additive manufacturing of HSLA steel: Effect of thermal cycles on microstructure and mechanical properties, *Addit. Manuf.*, 27(2019), p. 440.

[16] J. Goldak, A. Chakravarti, and M. Bibby, A new finite element model for welding heat sources, *Metall. Mater. Trans. B*, 15(1984), No. 2, p. 299.

[17] D.S. Liu, Y.M. Lü, W.J. Zhou, H. Yang, and K. Yang, Numerical simulation of temperature field in TIG arc additive manufacturing based on ANSYS, *Laser Optoelectron. Prog.*, 56(2019), No. 24, art. No. 241405.

[18] Y.M. Jing, Y.S. Zhang, W.K. Liang, X.Y. Zheng, and Y. Li, Effect of heating rate on austenitization of 22MnB5 ultra high strength steel, *Mater. Mech. Eng.*, 40(2016), No. 4, p. 80.

[19] J. Pu, S.F. Yu, and Y.Y. Li, Role of inclusions in flux aided backing submerged arc welding, *J. Mater. Process. Technol.*, 240(2017), p. 145.

[20] A.M. Guo, S.R. Li, J. Guo, P.H. Li, Q.F. Ding, K.M. Wu, and X.L. He, Effect of zirconium addition on the impact toughness of the heat affected zone in a high strength low alloy pipeline steel, *Mater. Charact.*, 59(2008), No. 2, p. 134.

[21] H.Q. Zhang, *Metallics of Steel Melt Welded Joint*, China Machine Press, Beijing, 2000, p. 301.

[22] Z.C. Liu, H.P. Ren, and Y.P. Ji, *New Theory of Solid Phase Transition*, Science Press, Beijing, 2015, p. 120.

[23] Z.Q. Cui and Y.C. Qin, *Metallography and Heat-Treatment*, China Machine Press, Beijing, 2007, p. 175.